Received: 28 November 2017 | Accepted: 1 February 2018

DOI: 10.1111/jace.15479

ORIGINAL ARTICLE

Journal of the American Ceramic Society

Zirconium carbide oxidation: Kinetics and oxygen diffusion through the intermediate layer

Claudia Gasparrini[1] | **Richard J. Chater**[2] | **Denis Horlait**[1,3] | **Luc Vandeperre**[2] | **William E. Lee**[1]

[1]Centre for Nuclear Engineering (CNE) & Department of Materials, Imperial College London, London, UK

[2]Department of Materials, Imperial College London, London, UK

[3]UMR 5797, CNRS, Centre D'Etudes Nucléaires de Bordeaux-Gradignan, Gradignan, France

Correspondence
Claudia Gasparrini, Centre for Nuclear Engineering (CNE) & Department of Materials, Imperial College London, London, UK.
Email: cg1614@ic.ac.uk

Funding information
Engineering and Physical Sciences Research Council, Grant/Award Number: DISTINCTIVE EP/L014041/1, Industrial Case Award EP/M507428/1

Abstract

Oxidation of hot-pressed ZrC was investigated in air in the 1073-1373 K range. The kinetics were linear at 1073 K, whereas at higher temperature samples initially followed linear kinetics before undergoing rapid oxidation leading to a Maltese cross shape of the oxide. The linear kinetics at 1073 K was governed by inward oxygen diffusion through an intermediate layer of constant thickness between ZrC and ZrO_2 which was comprised of amorphous carbon and ZrO_2 nanocrystals. Diffusion of oxygen through the intermediate layer was measured to be 9×10^{-10} cm^2 s^{-1} using ^{18}O as a tracer in a double oxidation experiment in $^{16}O/^{18}O$. Oxidation at 1073 and 1173 K produced samples made of m-ZrO_2 and either t- or c-ZrO_2 with an adherent intermediate layer made of amorphous carbon and ZrO_2, whereas oxidation at 1273 and 1373 K produced samples with a voluminous oxide made of m-ZrO_2 showing a gap between ZrC and the oxide. A substoichiometric zirconia layer was found at the gap at 1273 K and no carbon uptake was detected in this layer when compared with the top oxide layer. The loss of the intermediate layer and the slowdown of the linear rate constant (g m^{-2} s^{-1}) at 1273 K compared to 1173 K was correlated with the preferential oxidation of carbon at the intermediate layer which would leave as CO and/or CO_2 leaving a gap between ZrC and substoichiometric zirconia.

KEYWORDS
oxidation, zirconia, zirconium/zirconium compounds

1 | INTRODUCTION

Zirconium carbide has potential in ultrahigh-temperature applications such as for coatings on hypersonic vehicles[1,2] or as an inert matrix fuel in the nuclear industry.[3,4] ZrC has better properties than other carbides such as a higher thermal conductivity and higher melting point,[5-8] however, a comprehensive database on its properties is not available and therefore its use is rarely considered.[9]

The oxidation of ZrC has been studied[10-19] under several experimental conditions of temperature and pressure[10-14] but a clear understanding has not yet been achieved due to the large numbers of variables that affect it, such as chemical composition of the initial material (C/Zr stoichiometry), porosity, or grain size.[9,20]

A mechanistic model recently proposed by Katoh et al[9] building on the model previously proposed by Shimada[21] showed as an initial stage the formation of an oxycarbide

$ZrO_xC_{(1-x)}$ layer[9,10,22] prior to the formation of an oxide layer. This oxycarbide layer has, however, never been experimentally observed, perhaps because the ZrC crystal structure can accommodate up to 60% of oxygen in the crystal lattice without changing its structure.[22]

The overall reaction proposed by Katoh et al[9] and Rama Rao and Venugopal[22] is summarized as:

$$ZrC + \frac{1}{2}(1-x)O_2 \rightarrow ZrC_xO_{1-x} + (1-x)C \quad (1)$$

$$ZrC_xO_{1-x} + \frac{1}{2}(1+3x)O_2 \rightarrow ZrO_2 + (x)CO_2 \quad (2)$$

What is missing from the model proposed by Katoh et al[9] are the effects of formation of the different zirconia polymorphs and the influence of carbon oxidation on the oxide microstructure with temperature. Carbon is produced during either ZrC oxidation or $ZrO_xC_{(1-x)}$ oxidation and is considered to remain in the oxide layer as inclusions at low temperatures, from $653 < T < 873$, or to react with oxygen, above 870 K, leaving the system as CO/CO_2.[9]

The interface characterization between the carbide and the oxide on samples oxidized at 1073 K and the Maltese cross shape development was the topic of our previous publication.[23] The Maltese cross shape of the oxide is induced by crack development at sample corners during the initial stages of the reaction.[23] The failure of corners promotes rapid growth of the oxide in this region. The interface between the carbide/oxide of a hot-pressed ZrC specimen oxidized at 1073 K for 1 hour in air was comprised of a 2-μm-thick amorphous carbon matrix with ZrO_2 nanocrystals embedded in it. Based on this finding, the present work gives deeper understanding of the role of this interface in the reaction mechanism from 1073 to 1373 K for hot-pressed ZrC specimens. Macroscopic characterization via XRD and SEM of the oxide layer at different temperatures was coupled with the use of an isotopic exchange technique where oxygen diffusion was tracked by SIMS analysis using an isotopic tracer (^{18}O).

2 | EXPERIMENTAL PROCEDURE

High-density ZrC pellets were made using the same procedure described in ref,[23] where the description of Set A, B, and C samples can be found.[23] Commercial ZrC powder (3-5 μm; 90% < 8 μm with 0.2% < Hf < 2%; Grade B; H.C. Starck, Karlsruhe, Germany) has, according to the manufacturer, a carbon concentration of 11.6 wt% (with 11.1% being combined and 0.5% being free carbon). Set B ZrC pellets made from this powder in this study had a carbon concentration of 11.9% with an error ≤0.1% measured with an EMIA 320 V2 carbon and sulfur chemical analyzer (Horiba Scientific, Kyoto, Japan). The commercial ZrC powder analyzed with the same unit showed a carbon concentration of 11.7% with an error ≤0.1%, showing that Set B pellets acquired additional carbon on hot pressing. Set A ZrC pellets presented a carbon content of 11.2%. The same technique was used to quantify the carbon concentration in the oxide layer.

Samples from Set A, hot pressed at 2123 K, were used for characterization of the ZrC and ZrO_2 layers across their interface with a Focused Ion Beam instrument coupled with a Secondary Ion Mass Spectrometer (FEI FIB200-SIMS; FEI Company, Hillsboro, OR). This microscope uses a gallium source for imaging and sputtering. A high current (20 000 pA) was used to sputter the sample cross-sectional surface for 5 minutes, whereas imaging was performed at a current between 1000 and 3000 pA. SIMS chemical analysis was done on a 100 μm square region made of 10 rectangles of dimensions 10 μm × 100 μm across the interface sputtered at a current of 3000 pA. From each rectangle, secondary negative and positive ions were collected to evaluate the chemical abundance of carbon and oxygen species. On each rectangular area previously analyzed by SIMS, energy-dispersive X-ray spectrometer (EDX) chemical analysis was also performed with the INCA system (INCA; Oxford Instruments, UK) equipped with an ultrathin polymer window in a LEO Gemini 1525 FEGSEM (Zeiss, UK), at 20 kV. To evaluate the amount of material removed by the action of the FIB-SIMS a nondestructive technique was used: the Zygo NewView 200 3D optical interferometer which enables surface topography characterization. The sputter depth of the gallium source was approximately 0.6 μm in the ZrC side and 1.6 μm in the ZrO_2 side.

Set B, 1 cm^3 cubes, hot pressed at 2273 K, were used for kinetic analyses and oxide layer growth measurements. Chemical characterization with EDX on sample cross sections polished and coated with chromium was performed in a JSM 6400 (JEOL, USA). Characterization of the oxide layer was performed by X-ray diffraction (XRD) on a Bruker D2 Desktop (MA, USA), using a Cu Kα source. XRD was performed on oxide fragments or on powders, which were prepared by crushing the oxide layer with an agate pestle in an agate mortar. Quench treatments for kinetic analyses in a chamber-lift furnace were performed in air atmosphere at 1073, 1173, 1273, and 1373 K at times from 15 until 480 minutes. Prior to insertion in the furnace, the samples were weighed and placed in a zirconia or alumina crucible so that the monitoring of weight would not be affected by oxide layer spallation. At 1073 and 1173 K oxidation gave partly oxidized samples and the oxide layer measurements were performed in an optical microscope (Olympus UC30, Tokyo, Japan) on sample cross sections after cutting the samples in half with a diamond-copper saw (Isomet Low Speed Saw; Buehler, Braunschweig,

Germany). Oxide thickness was measured by averaging the measurements taken in the middle point of each side. The oxide layer in the samples oxidized at 1273 and 1373 K did not adhere to the carbide core but detached during handling, therefore the oxide thickness was estimated from the residual thickness measured using electronic calipers (accuracy of 0.01 mm) in the centre of the surface. Weight change and surface area measurements were recorded on samples before and after quenching. Kinetic evaluation was performed first by plotting the change in weight normalized per initial surface area and then by plotting the change in weight normalized per carbide core surface area of the carbide after quenching as a function of time. Data were then fitted according to Equations 3 and 4:

$$\frac{\Delta W}{A} = k_l t \tag{3}$$

$$\left(\frac{\Delta W}{A}\right)^2 = k_p t \tag{4}$$

where ΔW is the weight change after oxidation (g), A is the surface area (m^2), k_l and k_p are the linear (g m^{-2} s^{-1}) and parabolic (g^2 m^{-4} s^{-1}) rate constants, respectively, and t is the time (seconds).[24,25] The mass gain normalized per initial surface area takes into account the initial area of the manufactured ZrC sample, whereas the mass gain normalized per carbide surface area takes into account the area of the carbide sample core evaluated at each quench time. For experiments at 1273 and 1373 K the carbide core area was measured with the calipers as the oxide was not adherent. The area in this case is evaluated with Equation 5 or 6 depending on the shape of the carbide core which turned from a cuboid shape to a spherical one (see results section in our previous publication[23]).

$$A_{carbide} = 2(a \cdot b) + 2(b \cdot c) + 2(c \cdot a) \tag{5}$$

$$A_{carbide} = 4\pi r^2 \tag{6}$$

where a, b, and c are the dimensions of the cuboid and r in Equation 6 is the radius of the sphere. The carbide area for samples oxidized at 1073 and 1173 K was evaluated by subtracting the dimensions of the partly oxidized cube measured in the centre of each face using caliper from the oxide layer thickness evaluated with the optical microscope. For long oxidation times (>2 hours) the oxide layer grew drastically assuming the typical Maltese cross shape so the oxide thickness was measured in the center of the face of the cross section as this layer showed a compact structure.

In situ XRD analysis was performed on commercial ZrC powder using a high-temperature XRD (HT-XRD); X'pert Multi-Purpose Diffractometer (MPD; Philips, Amsterdam, the Netherlands) under air. Oxidation was simulated by heating the sample in air on a platinum holder (HDK 2.4; Buhler, Germany) at 40 kV and 40 mA, using Ni-filtered CuKα radiation between room temperature and 1306 K, with scans performed every 50 K.

Set C, cut from a Set B sample, was used for a double oxidation experiment using an ^{16}O followed by ^{18}O enriched atmosphere in an isotopic exchange set up. The sample was placed on a crucible inside a quartz furnace evacuated to 10^{-7} mbar, a flux of 200 mbar of oxygen was inserted when a temperature of about 1060 K was reached. The sample was first exposed to the oxygen atmosphere for 4 minutes in research-grade ^{16}O (mostly consisting of ^{16}O plus the natural ^{18}O abundance of 0.2%), then the furnace was evacuated and cooled before the second oxidation was performed in an atmosphere of 40% enriched ^{18}O gas at 200 mbar at the same temperature and time as the first oxidation.

FIB-SIMS was used to mill a ramp across the ZrC/ZrO_2 interface using an Oregon-Physics Plasma FIB (Hillsboro, OR) 500 nA/30 keV/Xe beam. This ramp had a slope of 26.6° and width of 150 μm. The roughness of the top surface was 5.2 μm. SIMS and EDX analysis (done in a LEO Gemini 1525 FEGSEM, at 20 kV) were performed on a ramp made with the FEI FIB200-SIMS in the center of this region. This final ramp used for analysis showed a 30° slope with a width of 45 μm and height of 40 μm. This ramp presented a smoother surface compared to the ramp milled by the Plasma FIB so that the SIMS data collected were less noisy. Point scan EDX was performed and errors were evaluated by averaging the values and taking the standard deviation of the measurements done on the same area. A MATLAB code was used to plot the SIMS data on the ramp. $^{18}O^-$ isotopic fraction, called here IF, is a useful tool[26] as it represents the oxygen isotope distribution on the surface and limits any sharp change in ion signal intensities due to sample topography or localized charging.[27] IF is evaluated with Equation 7:

$$IF = \frac{^{18}O^-}{^{16}O^- + ^{18}O^-} \tag{7}$$

where $^{16}O^-$ and $^{18}O^-$ represents the oxygen ions intensities detected by FIB SIMS.

3 | RESULTS AND DISCUSSION

3.1 | Oxidation kinetics

Figure 1A shows the mass gain normalized per initial surface area vs time of samples quenched from 1073 to 1373 K. Data initially were fitted to a parabolic law (Equation 4) as shown in Figure 1B. This first analysis is, however, misleading as it does not take into account the transformation of the carbide core surface area evolution which is known to be of primary importance in metal

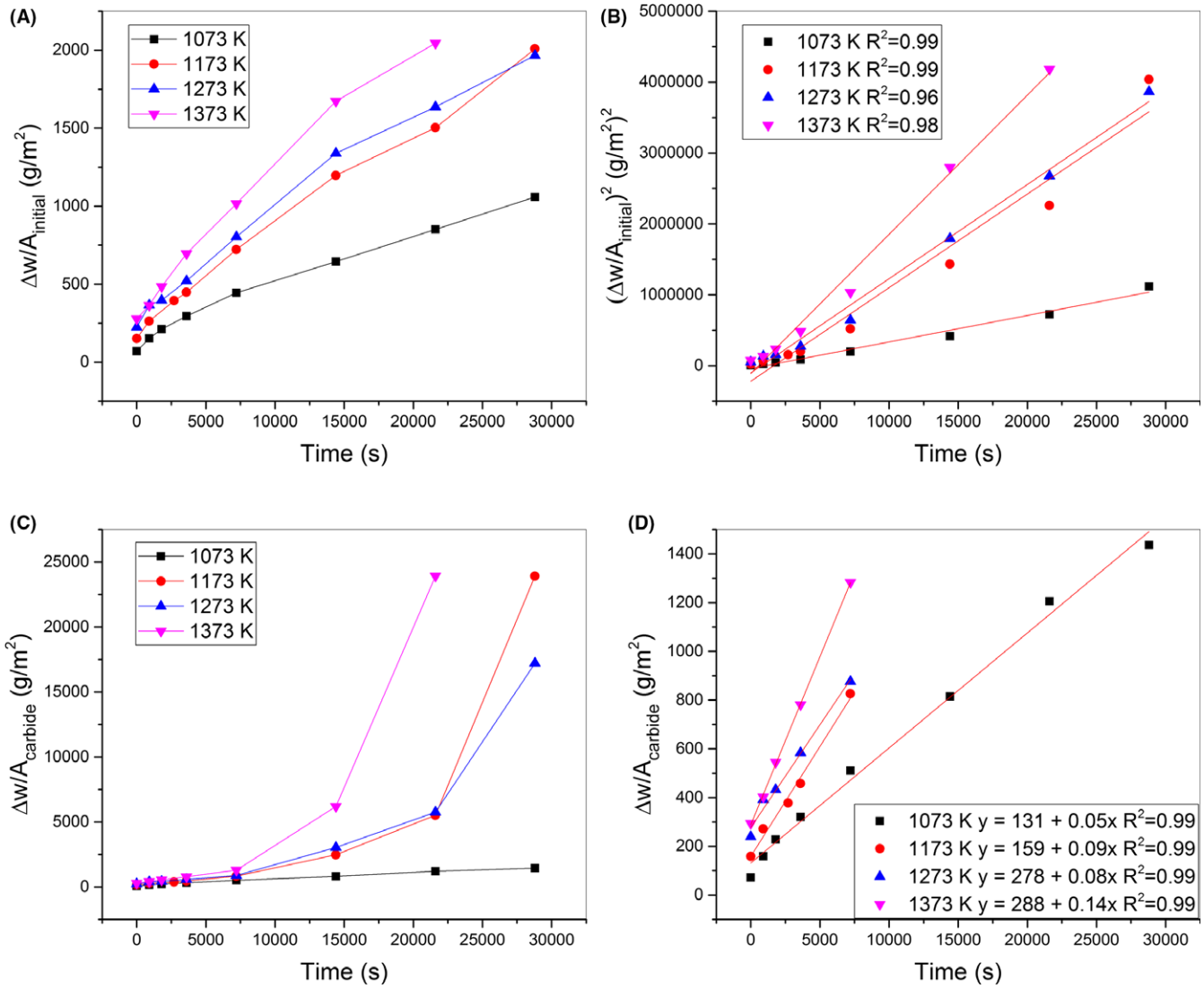

FIGURE 1 Plots of ZrC samples oxidized in 1 atm of oxygen at 1073-1373 K quenching at 900-1800-3600-7200-14 400-21 600-28 800 s. A, weight change normalized per initial surface area; B, square of weight change normalized per initial surface area showing parabolic fitting; C, weight change normalized per carbide core surface area showing 2 kinetic trends: linear up to 2 h (7200 s) followed by rapid oxidation for samples oxidized from 1173 to 1373 K; D, linear fitting of the data up to 2 h shown in C [Color figure can be viewed at wileyonlinelibrary.com]

oxidation.[28] We consider this to be even more important for oxidation which involves a Maltese cross evolution of the oxide as it affects dramatically the carbide core surface area. Figure 1C shows the mass gain normalized per carbide core area vs time. Data for oxidation at 1073 K can be fitted to one kinetic regime, whereas2 regimes are needed for samples oxidized at higher temperature (1173-1373 K). The kinetics at 1073 K are linear, whereas those at 1173, 1273, and 1373 K fit a linear trend up to 2 hours of oxidation (shown in Figure 1D) followed by a rapid change as the oxidation growth accelerates (Figure 1C). Oxidation at an accelerated rate is referred to as breakaway oxidation and is usually accompanied by loss of a protective oxide layer.[29] In this case, breakaway oxidation occurred when the Maltese cross shape of the oxide fully developed. The oxide growth in this region is severe and is accompanied by shrinkage of the unoxidized carbide core that changes from its initial cubic shape to a spherical one (see Gasparrini et al[23]). For oxidation times over 2 hours the increase in oxidation was linked to the shrinking of the carbide core which was found in the form of a sphere, at the same time the oxide develops with the characteristic Maltese cross shape.

The drastic change in the carbide core from a cubic into a spherical shape, described in our previous publication,[23] is explained with the fact that corners are the points where the oxidation proceeded more rapidly developing with the typical Maltese cross shape. The carbide core surface area

is considered the most suitable parameter to be used to derive kinetic analysis when compared with the initial surface area, compare Figures 1B vs 1D, as data points in Figure 1D showed very good agreement with a linear fitting, $R^2 \geq 0.99$. From the linear fitting of the data plotted in Figure 1D, it is possible to evaluate the linear rate

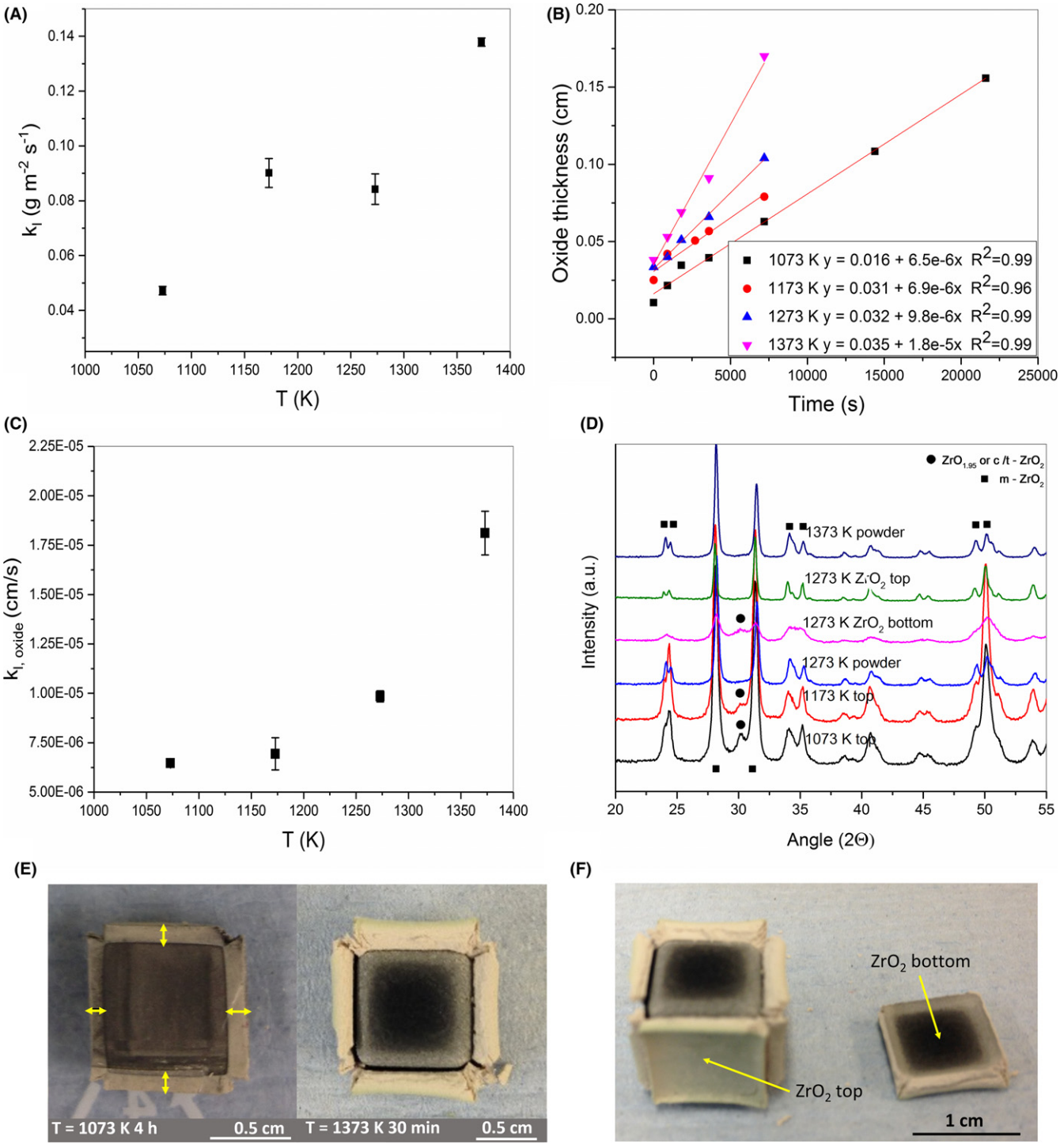

FIGURE 2 A, Plot of the linear rate constants (k_l) from Figure 1D as a function of temperature (T); B, plot of the oxide layer thickness vs time for ZrC oxidation at 1073-1373 K in air; C, plot of the oxide thickness linear rate constants ($k_{l,oxide}$) evaluated from the slope of straight lines in B; D, XRD characterization of ZrC hot-pressed specimens oxidized at 1073-1373 K in air, scans were performed either on top or bottom of the oxide layer: peaks are labeled as ■ for m-ZrO_2 or ● for t/c-ZrO_2 or $ZrO_{1.95}$.; E, photo of a partly oxidized ZrC sample cross section: (left) oxidized at 1073 K for 4 h showing the points where the oxide layer was measured (yellow arrows), (right) oxidized at 1373 K for 30 min showing the gap between the carbide and the oxide; F, sample shown in E (right) highlighting the points where XRD scans were done: top side (top ZrO_2 surface) and bottom side (black layer once in contact with ZrC) [Color figure can be viewed at wileyonlinelibrary.com]

constants, k_l, which are shown in Figure 2A. The linear rate constants do not show a clear trend: oxidation at 1073 and 1173 K showed an increase in oxidation rate but at 1273 K a slowdown occurred as the k_l is lower than at 1173 K. This slowdown in oxidation kinetics is accompanied by an increase in oxide thickness above 1273 K, as can be seen in Figure 2B,C. Figure 2B shows the oxide thickness vs time from 1073 to 1373 K, the slope of the straight lines fitting the oxide thickness rate are shown in Figure 2C and they are called the oxide thickness linear rate constants $k_{l,oxide}$. The oxide thicknesses have a similar growth rate at 1073 and 1173 K, however, at higher temperatures the rate of oxide layer growth increased considerably. The slowdown in kinetics at 1273 K which corresponds to an increase in oxide layer thickness was investigated through experimental observations. Specimens oxidized at 1073 and 1173 K presented an adherent oxide layer, which withstood cutting with a diamond saw (see photo in Figure 2E left). Samples oxidized at 1273 and 1373 K instead showed a voluminous oxide layer which was easily damaged during handling. The oxide layer was detached from the carbide core as a gap was present between the oxide and the carbide (see photos in Figure 2E right and Figure 2F).

XRD analysis was performed on the bottom side (once in contact with ZrC) and top side (exposed to air) of the oxide layer in samples oxidized at 1273 and 1373 K for 30 minutes as well as on the top surface of the oxide layer formed at 1073 and 1173 K for 30 minutes which was still adherent to the sample. XRD analysis on these samples showed that the oxide layer formed at 1273 and 1373 K was mostly made of m-ZrO_2, whereas at 1073 and 1173 K the oxide was made of m-ZrO_2 and either t/c-ZrO_2 (see Figure 2D).

A fine black powder was found between the carbide and oxide after oxidation at 1273 K and 1373 K and this could either be free carbon arising from the reaction happening at the interface, as previously reported by Voitovich and Pugach,[16] or substoichiometric zirconia formed by anion vacancies[30] reported to be black[31] which presents the peak at $2\theta = 30°$ observed in Figure 2D. The detached oxide layer had a black appearance on the bottom side, where it was once in contact with ZrC, and a white appearance on the top side. This is in agreement with the observation of Shimada et al[32] on ZrC single crystal oxidized at from 0.02 to 2 kPa partial pressure of oxygen, however, in our case the black layer could not be separated from the white layer. In some cases, the oxide was cracked and lifted in the centre as if some gases pushed to make their way out of the bulk, likely CO and/or CO_2.

The possibility that the oxide at 1073 and 1173 K could be comprised of either t- or c-ZrO_2 is due to the fact that the most common phase in the system is m-ZrO_2 which matches all the XRD peaks present in t- or c-ZrO_2 and $ZrO_{1.95}$ plus other peaks, apart from one at $2\theta = 30°$ which unfortunately is common with these phases (see PDF 037 1484[33] for m-ZrO_2, 050 1089[34] for t-ZrO_2, 049 1642[35] for c-ZrO_2, and 01 081 1544[36] for $ZrO_{1.95}$). An experimental observation on samples oxidized at 1073 and 1173 K showed that the oxide formed was compact and stress resistant. For example, during a TGA/DTA experiment at 1073 K, a partially oxidized sample underwent volume expansion and cracked the alumina crucible without any sign of crumbling. As a result it is plausible the peak at 30° is from tetragonal zirconia which is known to improve the strength and toughness of m-ZrO_2 when dispersed within it due to its ability to undergo a stress-induced polymorphic transfomation.[37] Rama Rao et al,[22] however, detected the cubic polymorph of zirconia below 1073 K during ZrC powder oxidation which then transformed to the monoclinic polymorph at higher temperatures. At equilibrium, pure c-ZrO_2 is stable at much higher temperatures than those investigated here, between 2640 K up to the melting point at 2950 K,[38] but other authors found the cubic polymorph during oxidation of ZrC at relatively low temperatures.[39] The identification of the second polymorph in this work is considered to be either t- and/or c-ZrO_2 due to the discrepancies found in literature and the difficulties of differentiating these 2 polymorphs with the available techniques (XRD, TEM) when the monoclinic polymorph is also present. Still it is evident that the second polymorph found in samples oxidized at 1073 and 1173 K enhances the capabilities of zirconia to sustain stresses.

XRD analysis on the crushed oxide layer formed during oxidation at 1273 K and 1373 K showed this to be comprised of m-ZrO_2 (see Figure 2D labeled as 1273 K powder), however, when XRD analysis was performed on the bottom and top sides of the oxide the XRD pattern changed. The bottom/black surface was comprised of both m-ZrO_2 and either t/c-ZrO_2 or substoichiometric $ZrO_{1.95}$. The black color can be explained either by carbon traces or by the presence of an oxygen-deficient m-ZrO_2 layer, identified by Sinhamahapatra et al[31] as ZrO_{2-x}. Substoichiometric zirconia could be difficult to imagine in a highly enriched oxygen atmosphere such as atmospheric air. It has been, however, previously reported during zirconium oxidation in an atmosphere of oxygen of 2×10^{-8} Torr by Ma et al.[40] The substoichiometric layer found by Ma et al,[40] called ZrO_x, was sandwiched between zirconium metal and stoichiometric ZrO_2. This 3-layered structure made of $Zr/ZrO_x/ZrO_2$ was considered energetically more stable to form than an interface Zr/ZrO_2.[40] In our study, the black layer next to ZrC was identified as substoichiometric zirconia because it well matched the $ZrO_{1.95}$ XRD pattern and its black appearance[31] could only be assigned to the presence of ZrO_{2-x} and not to carbon traces. Carbon

analysis was indeed performed on both the top white side and the bottom black side of the sample: both analyses revealed the same carbon content. Carbon analysis performed on a fragment taken from the white top side of a sample oxidized at 1273 K for 8 hours revealed a carbon content of 0.42 ± 0.01%, whereas the oxide black layer from a sample oxidized at 1273 K for 30 minutes, contained 0.42 ± 0.03% carbon. The sample oxidized for 8 hours was chosen so that it was possible to measure the carbon content (%) on the top side of the oxide layer far from the ZrC side. The sample oxidized for 30 minutes was chosen to have enough black layer to perform multiple analyses. The top side of the oxide was comprised of m-ZrO_2 as can be seen in Figure 2D. At higher temperatures, 1273 K, where the oxidation kinetics is slowed, we see that the intermediate layer is missing and the oxide next to this layer is substoichiometric zirconia. At the same time, the oxide thickness rate increases (see Figure 2C). The volume expansion from cubic to tetragonal and tetragonal to monoclinic is approximately +2%[41] and +4%,[42] respectively, therefore the voluminous and porous appearance of the oxide which grew thicker at 1273 and 1373 K compared to that formed after oxidation at 1073 and 1173 K could be explained by the stresses induced by these transformations. The apparent slowdown in the oxidation kinetics, k_l (measured in g m^{-2} s^{-1}) observed at 1273 K (see Figure 2A) could be related to either a mass gain rate decrease or a surface area increase. Results shown in our previous paper[23] showed that the surface area decreased over time during oxidation, therefore the slowdown in kinetics is related to a mass gain rate decrease. In carbides oxidation there is a competition between carbide oxidation and carbon oxidation (see Equations 8 and 9).

$$ZrC + O_2 \rightarrow ZrO_2 + C \quad (8)$$

$$C + O_2 \rightarrow CO_2 \quad (9)$$

During uranium carbide (UC) oxidation,[43] carbon oxidation occurs simultaneously with UC oxidation,[44] however, in the case of ZrC, previous work[18] suggests that CO/CO_2 is produced mostly during the cooling stage. In reference[18] the cracked sample surface was associated with the thermal expansion coefficient mismatch between the carbide and oxide polymorphs during the cooling stage. However, cracks were observed during the heating stage of the reaction using an in situ technique on ZrC[23] and UC.[43] These cracks would offer a route for CO/CO_2 to leave the sample during the heating stage. The mass gain rate decrease observed at 1273 K could be related to the loss of carbon due to carbon oxidation (Equation 9) over carbide oxidation (Equation 8). This occurs when reaction 9 prevails over reaction 8 or when carbon already present in the system is oxidized following reaction 9. Carbon oxidation is thought to prevail in the intermediate layer between ZrC/ZrO_2 for T = 1273 K following the results achieved on samples oxidized at 1073 K (where a layer of amorphous carbon was detected at the interface carbide/oxide, see Gasparrini et al[23]). The gap observed between the carbide and oxide for oxidations at 1273 and 1373 K could therefore be induced by preferential oxidation of carbon. Oxygen, when in contact with the intermediate layer made of carbon and zirconia, preferentially oxidizes the carbon that leaves the sample as CO or CO_2 via cracks through the porous oxide layer, as seen by Bellucci et al.[18] The preferential oxidation of carbon promotes an oxygen-deficient zirconia layer, characterized in this study with PDF 01 081 1544[36] for $ZrO_{1.95}$, to remain in the carbide/oxide gap. The substoichiometric zirconia is only found on the oxide next to the carbide in little amount, hence why it can only be detected when XRD is directly performed on the black surface of this oxide layer.

3.2 | In situ HT-XRD

Formation of t-/c-ZrO_2 below the generally accepted polymorphic stability ranges which start at 1448 K[45] for t-ZrO_2 and 2643 K[45] for c-ZrO_2 was confirmed during an oxidation experiment performed on ZrC powder in a high-temperature XRD. When ZrC powder is heated in a static air environment from room temperature to 1306 K (see Figure 3) the first oxide polymorph formed matched the t-/c-ZrO_2 pattern. The t-/c-ZrO_2 XRD pattern was seen from 891 to 1203 K, whereas for temperatures above this range m-ZrO_2 peaks appeared (XRD peaks were matched with PDF 037 1484[33] for m-ZrO_2, 050 1089[34] for t-ZrO_2, 049 1642[35] for c-ZrO_2 and PDF 035 0784[46] for ZrC).

There are several ways in which t-ZrO_2 can be stabilized over m-ZrO_2 including critical crystallite size and the presence of ion impurities or oxygen vacancies. Regarding the critical crystallite size, the formation of t-ZrO_2 before m-ZrO_2 can be explained with the theory of Garvie[47,48] which states that a "critical crystallite size" exists for ZrO_2. Below a size of 5-16 nm t-ZrO_2 crystals are favored over m-ZrO_2 crystals, whereas above a critical size of 30 nm m-ZrO_2 crystals are favored. This occurs because t-ZrO_2 crystals are stabilized due to their reduced crystal surface free energy[49] when compared with m-ZrO_2. Previously we showed[23] that the crystallites of ZrO_2 formed were approximately 10 nm in size which agrees well with the theory of Garvie.[48] Another mechanism proposed by different authors for the stabilization of t-ZrO_2 at lower temperatures, even down to room temperature, is the presence of oxygen ion vacancies.[45] The presence of stable tetragonal phase in bulk ZrO_2 has been explained by oxygen ion vacancies within the ZrO_2 lattice supposedly generated either at higher temperature or under vacuum.[45] Srinivasan

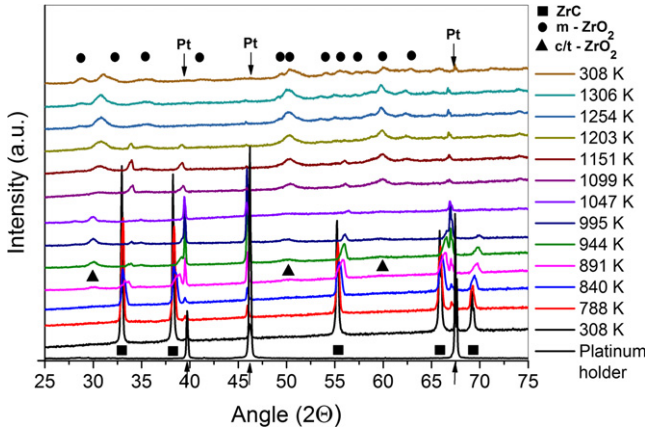

FIGURE 3 HT-XRD of ZrC powder oxidized from room temperature to 1306 K on a platinum foil with scans taken every 50 K under static air. The last scan was taken on the powder cooled to room temperature. Peaks were indexed using PDF 035 0784[46] for ZrC, PDF 037 1484[33] for m-ZrO_2, 050 1089[34] for t-ZrO_2, 049 1642[35] for c-ZrO_2 or compared to the platinum holder blank XRD pattern [Color figure can be viewed at wileyonlinelibrary.com]

et al[50] reported that the transformation from tetragonal to monoclinic ZrO_2 is related to the adsorption of gaseous oxygen at relatively low temperature, such as 573 K or on cooling during an HT-XRD study of zirconia. In our case the transformation from tetragonal to monoclinic occurs at high temperature, above 1099 K shown in Figure 3 and could be related to crystal growth or removal of oxygen vacancies from the ZrO_2 lattice. The characterization of a layer of substoichiometric zirconia on hot-pressed ZrC in samples oxidized at 1273 and 1373 K shown in Figure 2D suggests that the first oxide formed during ZrC oxidation is characterized by oxygen vacancies.

Previous studies of ZrC oxidation, typically identify the ZrO_2 crystallites as cubic[22,39,51] rather than tetragonal which, instead, is typically identified in amorphous ZrO_2 oxidation studies.[47,52] Due to this controversy and the similarities in their XRD patterns, as previously explained, both tetragonal and cubic polymorphs may be present in our system.

3.3 | Chemical analysis across the ZrC/ZrO_2 interface

A sample cross section (shown in Figure 4A) from set A oxidized in a furnace for 1 hour at 1073 K was analyzed by FIB-SIMS and SEM. Chemical analyses were performed by SIMS and EDX on each rectangle with size 100 × 10 μm highlighted in Figure 4A. SIMS is a surface characterization technique, whereas EDX gives information on the sample bulk. Figures 4B,C, and D show the normalized ions counted during SIMS analysis which are relevant to this system (expressed in fractions of counts per second: cps/cps): (B) carbon, (C) oxygen, and (D) zirconium-related species. SIMS analysis showed that on the ZrC side no oxygen was present and in the ZrO_2 side little carbon was found (see Figure 4B,C). In the same way the ions related to ZrC, in this case $ZrC_2(+)$, showed the highest yield in the ZrC side (see Figure 4D) and dramatically decreased to zero on the ZrO_2 side just 10 μm away from the carbide/oxide interface.

EDX performed on the same region after the FIB-SIMS analysis is shown in Figure 5A. EDX was done by selecting each 100 × 10 μm rectangle as previously done with SIMS, however, it was also performed outside the FIB SIMS sputtered region. Chemical analysis was performed considering all elements: no oxygen was found in the ZrC area and no carbon was found in the ZrO_2 side within the FIB-SIMS sputtered region as shown in Figure 5A (EDX peaks within this region are shown in Figure 5C). EDX performed outside the sputtered region reveals oxygen in the ZrC region and carbon in the ZrO_2 region. Gallium was present as it was used for FIB sputtering, however, it is neglected in the analysis as its abundance was ≤0.54 atomic (%).

The presence of oxygen in ZrC and carbon in the ZrO_2 side outside the FIB sputtered region could be related to contamination due either to the presence of an oxide layer (the sample was kept in air atmosphere) or to sample preparation effects (such as the effect of polishing or the chromium coating). Both SIMS and EDX analysis, however, are in agreement within the FIB-SIMS sputtered region that showed the presence of only ZrC and ZrO_2 on the left and right side of the interface region. EDX is well-known to lack sensitivity for light elements, such as carbon and oxygen, however, the similarities between the EDX and the SIMS analyses give EDX results credibility and this is why EDX is included in this work.

BSEI of sample cross sections (Figure 5B) show the 3 regions: ZrC (zone 1), intermediate layer (zone 2), and ZrO_2 (zone 3). Two samples from Set B oxidized at 1073 K were analyzed in BSE mode, the intermediate layer on the sample oxidized for 30 minutes was approximately 0.7-6.5 μm wide, whereas the intermediate layer in the sample oxidized for 4 hours at the same temperature was approximately 1.3-9.8 μm wide. An increase in the intermediate layer width occurs with time, however, this has an irregular thickness (see Figure 5B) and so the width is expressed as a range. EDX analysis for a sample oxidized for 30 minutes at 1073 K is shown in Figure 5D; oxygen was deliberately omitted in the analysis done on the ZrC side (zone 1) as the oxygen was found to be related to surface contamination in the analysis shown in Figure 5A. Chromium was also neglected in the analysis as the abundance of 0.51% arises from the chromium coating deposited during sample preparation. Two analyses were performed and the results are summarized in Table 1.

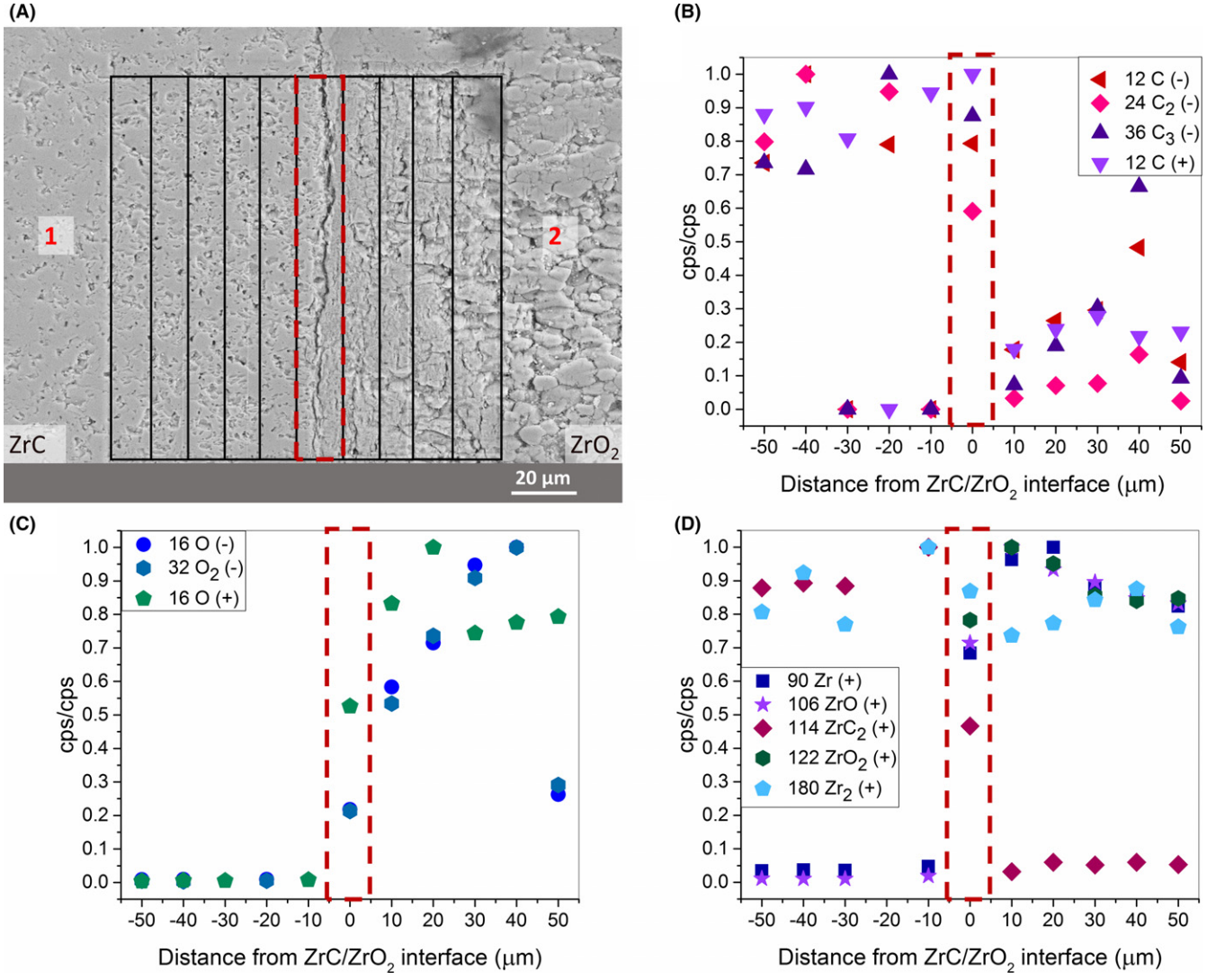

FIGURE 4 A, SEI of a sample cross section oxidized at 1073 K for 1 h (set A), the squared region divided into 10 rectangles of size 100 × 10 µm is the region where FIB-SIMS analysis was performed followed by EDX analysis, the dashed rectangle highlights the interface; normalized values for the (B) carbon-related secondary ions; C, oxygen-related secondary ions; D, zirconium-related secondary ions sputtered from the surface and expressed in cps/cps (counts per second) [Color figure can be viewed at wileyonlinelibrary.com]

EDX analysis shows that Zr and O are present in a stoichiometric ratio 1:2 in the oxide layer but also in the intermediate layer region. This result is in agreement with the observations performed via transmission electron microscopy where the intermediate layer was found to be comprised of ZrO_2 nanocrystals embedded in an amorphous carbon layer.[23] EDX also shows that the intermediate layer is comprised of carbon and ZrO_2.

3.4 | Oxygen tracer diffusion

An oxygen tracer technique was used to determine how oxygen combines with the carbide during ZrC oxidation. Figures 6A,C show the top view of the sample surface and the attempts made to create a ramp across the oxide layer suitable for SIMS analysis. The only successful ramp used for this study is highlighted and shown from the side in Figure 6B.

Figures 6D,E show a BSEI and a high magnification ion image of the ramp across the ZrC/ZrO_2 interface sputtered and polished by FIB. Figure 6E is the region used for SIMS analysis. The 3 regions observed: ZrC, intermediate layer and ZrO_2 are labeled as 1, 2, and 3, respectively. EDX chemical characterization on these regions is shown in Table 2. Figures 6F,G show the SIMS elemental mapping: Figure 6F shows the total oxygen abundance map across this region, whereas Figure 6G shows the $^{18}O^-$ isotopic fraction (IF) distribution on the same area. Figure 6F shows that the total oxygen, sum of both $^{16}O^-$ and $^{18}O^-$ ions, is evenly distributed across zone 3 apart from sharp changes

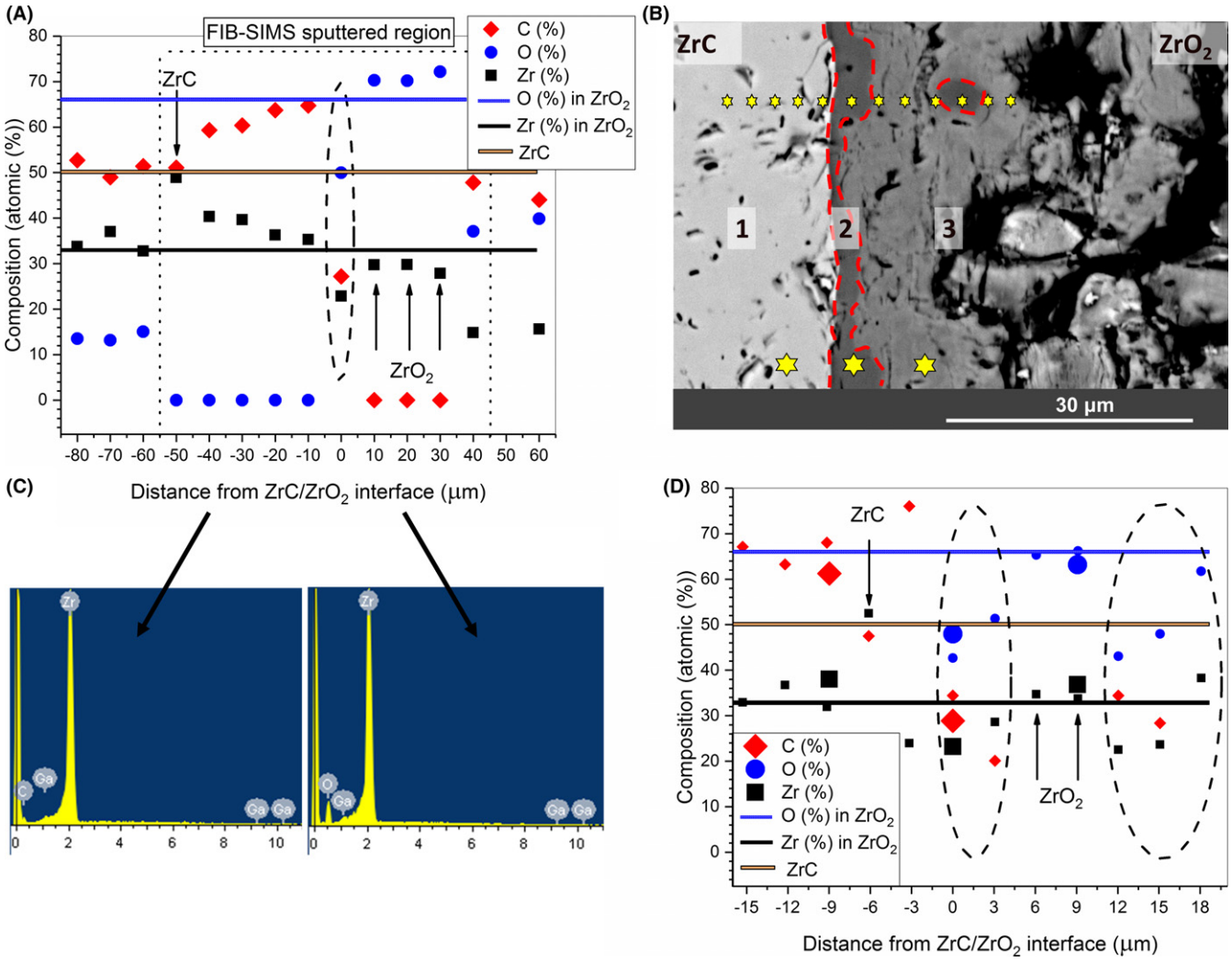

FIGURE 5 A, EDX analysis performed on each rectangle shown in Figure 4A after FIB-SIMS analysis showing composition in atomic (%), stripes show the stoichiometric values of ZrO_2 and ZrC; B, BSEI of a sample cross-section oxidized for 30 min at 1073 K (set B), red dashed lines highlight the interface region (dark zones) labeled as 2, zone 1 is ZrC, and zone 3 is ZrO_2, starred symbol highlights points where EDX was performed; C, example of EDX spectra acquired from the ZrC and ZrO_2 sides within the sputtered region; D, EDX analysis performed on each point labeled in B showing composition in atomic (%), the different size of the symbols refer to the 2 EDX analyses with 2 symbols sizes shown in B [Color figure can be viewed at wileyonlinelibrary.com]

TABLE 1 Chemical composition of the ZrC side, intermediate layer, and ZrO_2 side (labeled as 1, 2, and 3 in Figure 5B) of sample oxidized at 1073 K for 30 min. All data shown are in atomic (%)

ZrC side (1)		**Intermediate layer (2)**			**ZrO_2 (3)**		
Zr (%)	**C (%)**	**Zr (%)**	**O (%)**	**C (%)**	**Zr (%)**	**O (%)**	**C (%)**
37.6 ± 5.7	61.5 ± 6.1	22.7 ± 0.7	44.2 ± 2.4	33.2 ± 3.0	33.5 ± 2.9	62.8 ± 5.2	18.4 ± 1.7
C/Zr = 1.6 ± 0.3		O/Zr = 2 ± 0.2			O/Zr = 1.9 ± 0.2		

of intensities due to sample's uneven morphology at cracks and pores. Figure 6G reveals a gradient of $^{18}O^-$ throughout zone 2, this intermediate layer is 5.8-16.9 µm wide (measured from Figure 6E). To characterize the IF gradient through the intermediate layer, an IF profile was computed by an integrated linescan method in MATLAB and this is shown in Figure 6H. This method consisted in evaluating an averaged value of the IF within a region, highlighted with a black square in Figure 6G, which was chosen as the border between zones 2 and 3 runs parallel to the border between zones 1 and 2. From the overall IF profile across zones 1, 2, and 3 shown in Figure 6H, the IF gradient

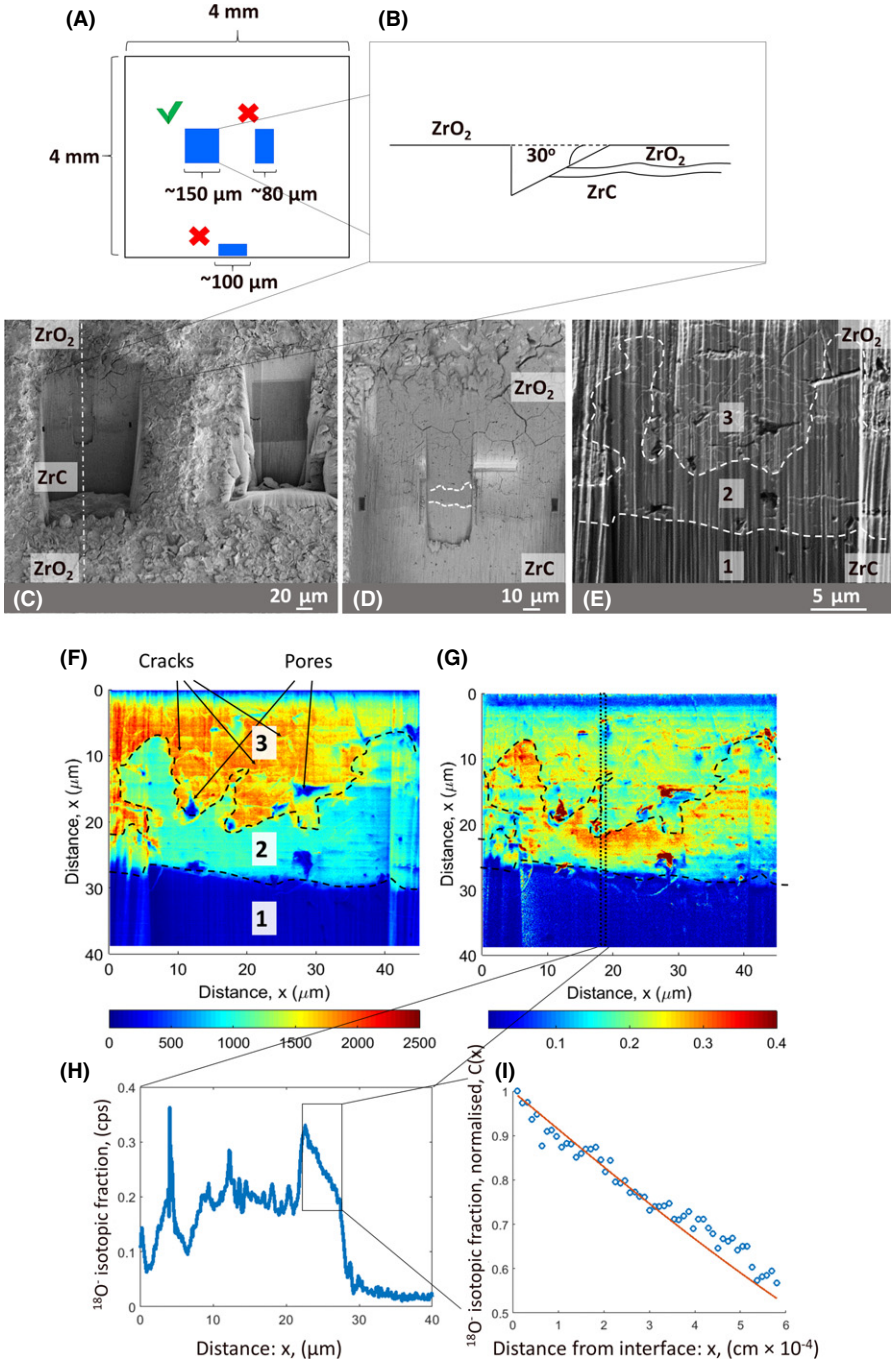

FIGURE 6 A, Top view image of the ZrC sample oxidized in $^{16}O/^{18}O$ environment: only the Plasma FIB ramp, 150 µm wide, was suitable for chemical analysis; B, side view representation of the ramp; C, SEI of the ramps milled on the top surface of the sample; D, BSEI of the Plasma FIB ramp, cracks are visible on the oxide surface; E, high magnification ions FIB image showing zones 1, 2, and 3 (ZrC, intermediate layer, ZrO_2, respectively); F, total oxygen map across the area seen in E; G, isotopic fraction, IF, $^{18}O/(^{16}O + {}^{18}O)$ map, the black dashed rectangle highlights the area where the averaged IF was calculated; H, averaged IF profile from the region highlighted in G; I, IF profile from zone 2 fitted with the Fick's law equation [Color figure can be viewed at wileyonlinelibrary.com]

across zone 2 was isolated and highlighted with a box in Figure 6H. This was normalized to 1 and is shown in Figure 6I. This profile was fitted using the Fick's second law of diffusion for a semi-infinite media, considering a constant source of gas[27] (Equation 10):

$$C'(x) = \frac{C(x) - C_{bg}}{C_g - C_{bg}} = \mathrm{erfc}\left(\frac{x}{2\sqrt{Dt}}\right) \quad (10)$$

where $C'(x)$ is the isotopic fraction which is normalized to the natural ^{18}O isotopic abundance, C_{bg} is equal to 0.2% and the gas tracer concentration C_g during the second anneal is equal to 40%. The parameter x represents the thickness of the intermediate region where the diffusion profile is measured, this is highlighted with the black box in Figure 6H, where $x = 0$ represents the border between zone 3 and 2 within the rectangle shown in Figure 6G; t represents the time of sample exposure to the oxidizing gases and D is the diffusion coefficient. The obtained diffusion coefficient D was $= 9 \times 10^{-10}$ cm^2 s^{-1} with $R^2 = 0.93$.

The diffusion coefficient for oxygen through this intermediate region in between ZrC/ZrO_2 is larger than the grain-boundary diffusion coefficients which is approximately $D_B = 1 \times 10^{-11}$ cm^2 s^{-1} evaluated by Brossmann

TABLE 2 Chemical composition of the ramp shown in Figure 6E: ZrC (zone 1), intermediate layer (zone 2), and ZrO_2 (zone 3) for ZrC sample oxidized at 1073 K in an isotopic exchange setup for 4 + 4 min first in ^{16}O then in a ^{18}O atmosphere. All data shown are in atomic (%)

ZrC side (1)			Intermediate layer (2)			ZrO_2 (3)		
Zr (%)	O (%)	C (%)	Zr (%)	O (%)	C (%)	Zr (%)	O (%)	C (%)
45.1 ± 4.0	7 ± 2.5	46.2 ± 4.8	27.2 ± 3.2	42.8 ± 1.8	28.9 ± 3.0	34.0 ± 2.5	61.5 ± 4.5	15.8 ± 2.6
C/Zr = 1.0 ± 0.1			O/Zr = 1.6 ± 0.1			O/Zr = 1.8 ± 0.2		

et al[53] with undoped ultrafine monoclinic ZrO_2 at 1073 K. The discrepancy with the value of Brossmann et al[53] can be explained by the fact that their ZrO_2 crystals were an order of magnitude larger than those present in our sample, 70-300 nm[53] compared to 10 nm (see TEM characterization in our previous paper[23]). The ^{18}O diffusion coefficient evaluated in this work, however, is representative of the oxygen diffusion through an intermediate layer where oxygen not only diffuses but also reacts to either form ZrO_2 nanocrystals[23] and/or CO/CO_2.

No ^{18}O gradient is present in zone 3 and therefore it is plausible that during the second oxidation step, either ^{18}O passed through an almost stoichiometric zirconia layer without significantly reacting with it or no diffusion gradient is present here due to the porous nature of the oxide layer. Confirmation of the stoichiometric nature of ZrO_2 is given by EDX analysis on the oxide layer just a few micrometers away from the intermediate layer (see Table 2). The porous and cracked nature of this oxide indicates that oxidation proceeded along grain boundaries,[23] and cracks are clearly visible in Figures 6D,E. Closer to the intermediate layer, zone 2, cracks are less pronounced compared with the cracks seen by SEM on polished surfaces which extend to 20 μm from the carbide/oxide interface (compare cracks in Figures 6E,D). SIMS analysis suggests that oxidation proceeded with inward formation of the oxide layer by oxygen penetration through cracks. The cracks present in the oxide layer mostly followed the grain boundaries (see Gasparrini et al[23] and cracks in Figure 6D), they are induced either by tension related to the volume expansion occurring in the transformation between ZrC to ZrO_2 or by stresses related to gas effusion when C oxidizes into CO/CO_2. The fact that the kinetics of oxidation of ZrC are linear, (see Section 3.1), is in agreement with the observation of the intermediate layer where oxygen diffusion needs to take place before this carbon-enriched layer can transform into ZrO_2. The cyclic debonding of this intermediate layer evidenced in a previous paper[23] shows the paramount role of this layer which acts as a diffusion barrier in the oxidation of ZrC at 1073 K in oxygen. A schematic of what is deduced to happen during hot-pressed ZrC oxidation is shown in Figure 7.

At 1073 and 1173 K an oxide made of m-ZrO_2 and t- and/or c-ZrO_2 developed adherent to the ZrC core via an intermediate layer made of amorphous carbon and nanocrystals of zirconia (this is schematically shown as a gray layer in Figure 7 top row between ZrC and the oxide; the characterization of this intermediate layer is shown in Gasparrini et al[23] in a sample oxidized at 1073 K). The oxide layer developed via the inward diffusion of oxygen through this intermediate layer. Diffusion of oxygen was measured to be 9×10^{-10} cm^2 s^{-1} using ^{18}O as a tracer in a double oxidation experiment in $^{16}O/^{18}O$ with SIMS. Diffusion took place in a layer of constant thickness, as the oxide cyclically debonds after reaching a thickness of approximately 20 μm (see Gasparrini et al[23]), in agreement with the linear kinetic observed at 1073 K (see Figure 1D). Diffusion is usually described with a parabolic behavior, in this case, however, the overall reaction rate was observed to be linear. Linear reaction rates can be ascribed to either a surface reaction or a diffusion mechanism through a protective layer of constant thickness.[29] Oxidation at 1173, 1273, and 1373 K followed linear kinetic up to approximately 2 hours where a drastic oxidation was related to the ZrC core change in shape from a cube to a sphere. Increasing the temperature to 1273 and 1373 K affected both the oxide morphology and the intermediate layer, as shown in Figure 7 bottom row. The oxide at 1273 and 1373 K was made of m-ZrO_2 and it was voluminous compared to the oxide formed at 1073 and 1173 K as the oxide thickness linear rate constants increased considerably (see Figure 2C). The voluminous nature of the oxide at 1273 and 1373 K can be explained with the volume expansion occurring between t/c-ZrO_2 and m-ZrO_2 which is usually reported to be approximately 4%.[42] Between ZrC and the oxide, a gap replaced the intermediate layer which was characterized at 1073 K. The oxide surface at 1273 K at the gap was characterized as substoichiometric zirconia (shown in Figure 7 as a yellow/gray ZrO_{2-x} layer), with no carbon uptake between this region and the top oxide surface. The decrease in linear rate constant, k_l ($g\ m^{-2}\ s^{-1}$), at 1273 K compared to 1173 K was related to the loss of carbon. Carbon could leave the system as CO and/or CO_2 due to preferential oxidation of carbon at the intermediate layer, reaction (9) prevailing over reaction (8), leaving a substoichiometric layer of ZrO_2 near the interface ZrC/ZrO_2.

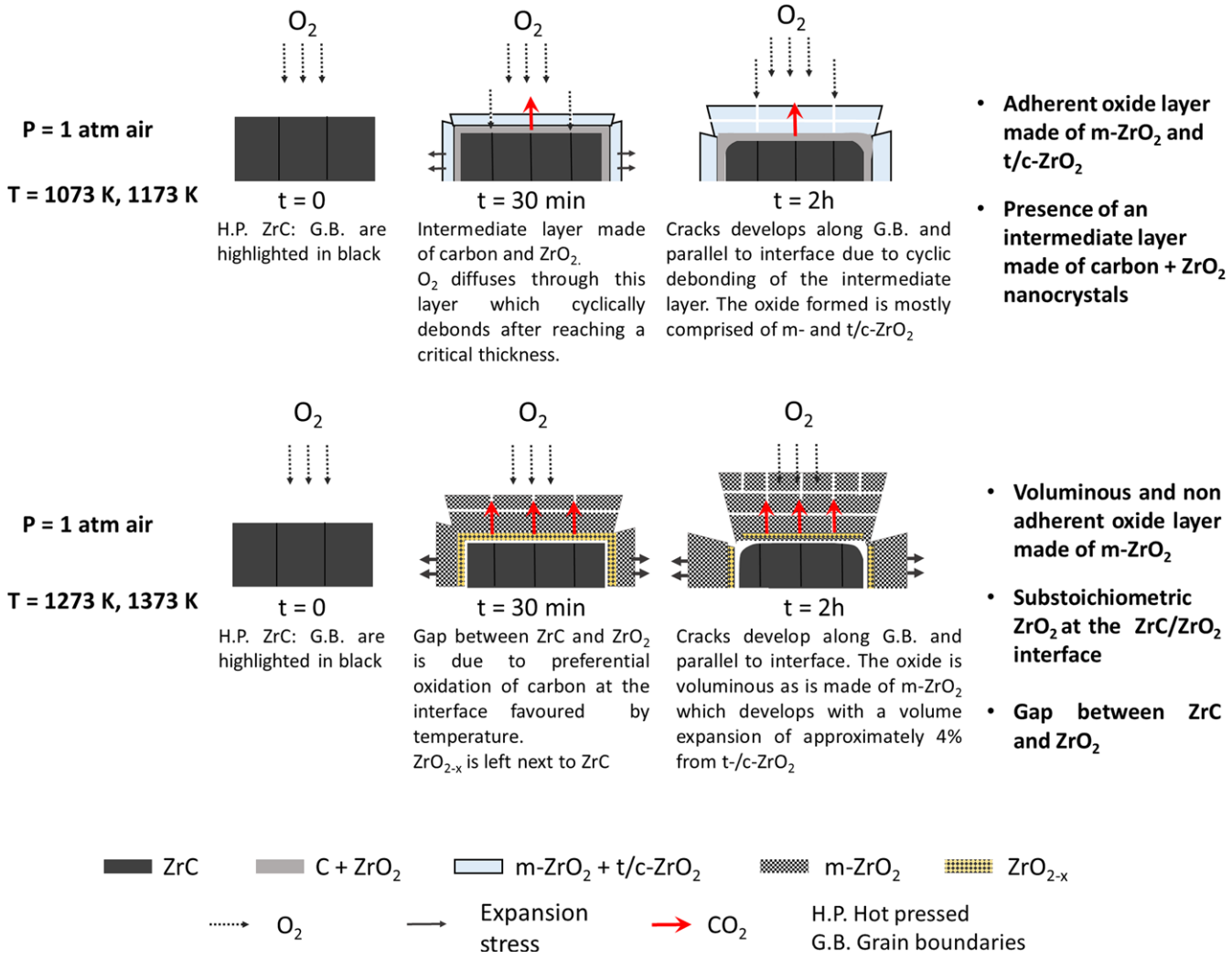

FIGURE 7 Oxidation stages of hot-pressed (H.P.) specimens of ZrC: at 1073 and 1173 K the oxide made of m-ZrO_2 and t/c-ZrO_2 develops attached to an intermediate layer comprised of amorphous carbon and ZrO_2 nanocrystals. The oxide is adherent and well sustains stresses. At 1273 and 1373 K the kinetics is slowed down by carbon oxidation in the intermediate layer that leaves a gap between the carbide core and the substoichiometric zirconia layer. The oxide layer is made of m-ZrO_2 and is voluminous, no adherent intermediate layer is observed [Color figure can be viewed at wileyonlinelibrary.com]

4 | CONCLUSIONS

The key role of the intermediate layer between ZrC and ZrO_2 during ZrC oxidation has been investigated.

1. Oxygen diffusion at 1073 K through the compact intermediate layer made of ZrO_2 nanocrystals and amorphous carbon was revealed by a double oxidation experiment performed in ^{16}O and ^{18}O atmosphere on a ZrC hot-pressed sample.
2. The diffusion coefficient measured with the use of ^{18}O as a tracer across the intermediate layer was 9×10^{-10} $cm^2\ s^{-1}$, $R^2 = 0.93$. The diffusion of oxygen through the intermediate layer made of nanocrystals zirconia and carbon is considered the rate-limiting step of the reaction.
3. This intermediate layer was observed to cyclically debond when a critical thickness is reached (approximately 20 μm). The overall linear kinetics of hot-pressed ZrC samples agrees with the oxidation mechanism governed by oxygen diffusion through a layer of constant thickness.
4. Linear rate constants (g $m^{-2}\ s^{-1}$) showed a slowdown at 1273 K compared to 1173 K, this was experimentally correlated with the loss of the intermediate layer made of carbon. Instead of the intermediate layer, a gap between the carbide core and the oxide was observed on samples oxidized at 1273 K as well as at 1373 K. Carbon loss at the intermediate layer was correlated with carbon oxidation prevailing over zirconium oxidation (Equation 9 prevails over Equation 8) which would leave the intermediate layer as CO and/or CO_2.

5. At the gap on samples oxidized at 1273 and 1373 K the oxide layer was black and it was identified as sub-stoichiometric zirconia as no carbon uptake was detected in the black oxide formed at 1273 K next to the ZrC side compared to the top white surface of the oxide layer at the same temperature.
6. Samples oxidized at 1273 and 1373 K showed a gap between ZrC and ZrO_{2-x} and the oxide was voluminous and made of m-ZrO_2. On the contrary, the oxide formed by oxidation at 1073 and 1173 K strongly adhered to the carbide core and was comprised of m- and t/c-ZrO_2.
7. The voluminous and heavily cracked structure of the oxide at 1273 K and 1373 K demonstrates its nonpassivating nature and explains the oxide thickness increase at these temperatures. Linear kinetics were followed by a drastic increase in oxidation after 2 hours of oxygen exposure for T = 1173-1373 K. This change was experimentally linked to the carbide core having its initial cubic shape evolving to a spherical one.
8. Cracking of the oxide and cyclic cracking of the intermediate layer is key for understanding the oxidation mechanism of ZrC. An analytical model and a finite element modeling (FEM) approach will be developed to assess the extent of stresses in the oxide during oxidation.
9. Rapid oxidation produced voluminous and heavily cracked oxides for oxidation from 1073 to 1373 K, hence, ZrC is not suitable for applications in oxygen environments in this range of temperatures.

ACKNOWLEDGMENTS

The authors are grateful to the EPSRC DISTINCTIVE (Decommissioning, Immobilization and Storage soluTIons for NuClear wasTe InVEntories) Consortium for their financial support of this project (EPSRC Industrial Case Award EP/M507428/1 Grant and the DISTINCTIVE EP/L014041/1 Grant). We also thank Dr Mahmoud Ardakani and Dr Ecaterina Ware for help with SEM-EDX analyses, Richard Sweeney for help with HT-XRD, Dr Michele Pettinà for developing a finite element modeling code simulating oxidation of ZrC, Dr Catriona McGilvery for help in characterize t- and/or c-ZrO_2 nanocrystals and Garry Stakalls for help with sample preparation.

ORCID

Claudia Gasparrini http://orcid.org/0000-0001-8343-4733
Denis Horlait http://orcid.org/0000-0002-2645-6896

REFERENCES

1. Paul A, Jayaseelan DD, Venugopal S, et al. UHTC composites for hypersonic applications. *Bull Am Ceram Soc*. 2012;91:22-29.
2. Wuchina E, Opila E, Opeka M, Fahrenholtz W, Talmy I. UHTCs : ultra-high temperature ceramic materials for extreme environment applications. *Electrochem Soc Interface*. 2007;16:30-36.
3. Lee WE, Gilbert M, Murphy ST, Grimes RW. Opportunities for advanced ceramics and composites in the nuclear sector. *J Am Ceram Soc*. 2013;96:2005-2030.
4. Minato K, Ogawa T, Fukuda K, et al. Fission product release from ZrC-coated fuel particles during postirradiation heating at 1600 C. *J Nucl Mater*. 1995;224:85-92.
5. Jackson HF, Jayaseelan DD, Manara D, Casoni CP, Lee WE. Laser melting of zirconium carbide: determination of phase transitions in refractory ceramic systems. *J Am Ceram Soc*. 2011;94:3561-3569.
6. Sara RV. The system zirconium-carbon. *J Am Ceram Soc*. 1965;48:243-247.
7. Manara D, Jackson HF, Perinetti-Casoni C, et al. The ZrC–C eutectic structure and melting behaviour: a high-temperature radiance spectroscopy study. *J Eur Ceram Soc*. 2013;33:1349-1361.
8. Jackson HF, Lee WE. Section 2.13 Properties and characteristics of ZrC. In: Konings JM, ed. *Comprehensive Nuclear Materials*, Vol. 2. Oxford, UK: Elsevier; 2012:339-372.
9. Katoh Y, Vasudevamurthy G, Nozawa T, Snead LL. Properties of zirconium carbide for nuclear fuel applications. *J Nucl Mater*. 2013;441:718-742.
10. Shimada S, Ishii T. Oxidation kinetics of zirconium carbide at relatively low temperatures. *J Am Ceram Soc*. 1990;73:2804-2808.
11. Shevchenko AS, Lyutikov RA, Andrievskii RA, Terekhova VA. Oxidation of zirconium and niobium carbides. *Sov Powder Metall Met Ceram*. 1980;19:48-52.
12. Bartlett RW, Wadsworth ME, Cutler IB. The oxidation kinetics of zirconium carbide. *Trans Metall Soc AIME*. 1963;227:467-472.
13. Barnier P, Thevenot F. A comparative study of the oxidation resistance of zirconium carbide and zirconium oxycarbide. *Eur J Solid State Inorg Chem*. 1988;25:495-508.
14. Janowski KR, Carnahan RD, Rossi RC. Static and dynamic oxidation of ZrC. Laboratory Operations Aerospace Corporation Report no TDR-669(6250-10)-3; 1966.
15. Berkowitz-Mattuck JB. High-temperature oxidation; IV Zirconium and hafnium carbides. *J Electrochem Soc*. 1967;114:1030-1033.
16. Voitovich RF, Pugach EA. High temperature oxidation of ZrC and HfC. *Sov Powder Metall Met Ceram*. 1973;12:916-921.
17. Gozzi D, Montozzi M, Cignini PL. Oxidation kinetics of refractory carbides at low oxygen partial pressures. *Solid State Ionics*. 1999;123:11-18.
18. Bellucci A, Gozzi D, Kimura T, Noda T, Otani S. Zirconia growth on zirconium carbide single crystals by oxidation. *Surf Coat Technol*. 2005;197:294-302.
19. Kuriakose AK, Margrave JL. The oxidation kinetics of zirconium diboride and zirconium carbide at high temperatures. *J Electrochem Soc*. 1964;111:827.
20. Hou X-M, Chou K-C. Investigation of the effects of temperature and oxygen partial pressure on oxidation of zirconium carbide using different kinetics models. *J Alloys Compd*. 2011;509:2395-2400.
21. Shimada S. Oxidation and mechanism of single crystal carbides with formation of carbon. *J Ceram Soc Jpn*. 2001;109:S33-S42.
22. Rama Rao GA, Venugopal V. Kinetics and mechanism of the oxidation of ZrC. *J Alloys Compd*. 1994;206:237-242.

23. Gasparrini C, Podor R, Horlait D, Chater R, Lee WE. Zirconium carbide oxidation: maltese cross formation and interface characterization. *Oxid Met*. 2017;88:509-519.
24. Harrison RW, Lee WE. Mechanism and kinetics of oxidation of ZrN Ceramics. *J Am Ceram Soc*. 2015;9:1-9.
25. Singhal SC. Thermodynamics and kinetics of oxidation of hot-pressed silicon nitride. *J Mater Sci*. 1976;11:500-509.
26. De Souza RA, Zehnpfenning J, Martin M, Maier J. Determining oxygen isotope profiles in oxides with Time-of-Flight SIMS. *Solid State Ionics*. 2005;176:1465-1471.
27. Foss BJ, Hardy MC, Child DJ, McPhail DS, Shollock BA. Oxidation of a commercial nickel-based superalloy under static loading. *J Miner Met Mater Soc*. 2014;66:2516-2524.
28. Mrowec S. Stokłosa a. Calculations of parabolic rate constants for metal oxidation. *Oxid Met*. 1974;8:379-391.
29. Kofstad P. *High Temperature Corrosion*. London & New York: Elsevier Applied Science; 1988.
30. Douglass DL. Corrosion mechanism of zirconium and its alloys—Diffusion of oxygen in zirconium dioxide. *Rep GEAP-3999, US At Energy Comm.*; 1962, Vol. 1.
31. Sinhamahapatra A, Jeon J-P, Kang J, Han B, Yu J-S. Oxygen-deficient zirconia (ZrO_{2-x}): a new material for solar light absorption. *Sci Rep*. 2016;6:27218.
32. Shimada S, Yoshimatsu M, Inagaki M, Otani S. Formation and characterization of carbon at the ZrC/ZrO_2 interface by oxidation of ZrC single crystals. *Carbon*. 1998;36:1125-1131.
33. McMurdie HF, Morris MC, Evans EH, Paretzkin B, Wong-Ng W, Hubbard CR. Standard X-Ray diffraction powder patterns from the JCPDS research associateship. *Powder Diffr*. 1986;1:265-275.
34. Málek J, Beneš L, Mitsuhashi T. Powder diffraction data and Rietveld refinement of metastable t-ZrO_2 at low temperature. *Powder Diffr*. 1997;12:96-98.
35. Tomaszewski H, Godwod K. Influence of oxygen partial pressure on the metastability of undoped zirconia dispersed in alumina matrix. *J Eur Ceram Soc*. 1995;15:17-23.
36. Martin U, Boysen H, Frey F. Neutron powder investigation of tetragonal and cubic stabilized zirconia, TZP and CSZ, at temperatures up to 1400 K. *Acta Crystallogr B*. 1993;49:403-413.
37. Gupta TK, Lange FF, Bechtold JH. Effect of stress-induced phase transformation on the properties of polycrystalline zirconia containing metastable tetragonal phase. *J Mater Sci*. 1978;13:1464-1470.
38. Howard CJ, Hill RJ, Reichert BE. Structures of ZrO_2 polymorphs at room temperature by high-resolution neutron powder diffraction. *Acta Crystallogr B*. 1988;44:116-120.
39. Shimada S, Nishisako M, Inagaki M, Yamamoto K. Formation and microstructure of carbon—containing oxide scales by oxidation of single crystals of zirconium carbide. *J Am Ceram Soc*. 1995;78:41-48.
40. Ma W, Herbert FW, Senanayake SD, Yildiz B. Non-equilibrium oxidation states of zirconium during early stages of metal oxidation. *Appl Phys Lett*. 2015;106:101603.
41. Kelly JR, Denry I. Stabilized zirconia as a structural ceramic: an overview. *Dent Mater*. 2008;24:289-298.
42. Guazzato M, Albakry M, Ringer SP, Swain MV. Strength, fracture toughness and microstructure of a selection of all-ceramic materials. Part II. Zirconia-based dental ceramics. *Dent Mater*. 2004;20:449-456.
43. Gasparrini C, Podor R, Horlait D, Rushton MJD, Fiquet O, Lee WE. Oxidation of UC: an in situ high temperature environmental scanning electron microscopy study. *J Nucl Mater*. 2017;494:127-137.
44. Iyer VS, Mukerjee SK, Kamat RV, et al. Oxidation behavior of carbide fuels. *Nucl Technol*. 1990;91:388-393.
45. Shukla S, Seal S. Mechanisms of room temperature metastable tetragonal phase stabilisation in zirconia. *Int Mater Rev*. 2005;50:45-64.
46. Morris MC, McMurdie HF, Evans EH, et al. Standard X-ray diffraction powder patterns. Section 21—Data for 92 substances. *Natl Bur Stand*. 1985;21:135.
47. Garvie RC. Stabilization of the tetragonal structure in zirconia microcrystals. *J Phys Chem*. 1978;82:218-224.
48. Garvie RC. The occurrence of metastable tetragonal zirconia as a crystallite size effect. *J Phys Chem*. 1965;69:1238-1243.
49. McGilvery CM. Nucleation and crystallisation of hafnium compounds and thin films. PhD Thesis, Imperial College, London; 2008.
50. Srinivasan R, Davis BH, Cavin OB, Hubbard CR. Crystallization and phase transformation process in zirconia: an in situ high-temperature X-ray diffraction study. *J Am Ceram Soc*. 1992;75:1217-1222.
51. Shimada S, Inagaki M, Suzuki M. Microstructural observation of the ZrC-ZrO_2 interface formed by oxidation of ZrC. *J Mater Res*. 1996;11:2594-2597.
52. Zhang F, Chupas PJ, Lui SLA, et al. In situ study of the crystallization from amorphous to cubic zirconium oxide: Rietveld and reverse Monte Carlo analyses. *Chem Mater*. 2007;19:3118-3126.
53. Brossmann U, Wurschum R, Sodervall U, Schaefer H-E. Oxygen diffusion in ultrafine grained monoclinic ZrO_2. *J Appl Phys*. 1999;1999:7646-7654.

How to cite this article: Gasparrini C, Chater RJ, Horlait D, Vandeperre L, Lee WE. Zirconium carbide oxidation: Kinetics and oxygen diffusion through the intermediate layer. *J Am Ceram Soc*. 2018;101:2638–2652. https://doi.org/10.1111/jace.15479